Boosting oxygen evolution in seawater media at large current density *via* boron-doped (Ni,Fe)OOH grown on Ni$_3$N nanosheets

Xin Xiao [a,b,c], Yan Wei [a], Shaowei Song [b], Brian McElhenny [b], Fanghao Zhang [b], Xingxing Jiang [a], Yang Zhang [a], Shuo Chen [b], Mingkui Wang [a], Yan Shen [a,*], Zhifeng Ren [b,*]

[a] *Wuhan National Laboratory for Optoelectronics, Huazhong University of Science and Technology, Wuhan 430074, China*
[b] *Department of Physics and Texas Center for Superconductivity at the University of Houston (TcSUH), University of Houston, Houston, TX 77204, USA*
[c] *Shenzhen Key Laboratory of Micro/Nano-Porous Functional Materials (SKLPM), SUSTech-Kyoto University Advanced Energy Materials Joint Innovation Laboratory (SKAEM-JIL), Department of Chemistry, Southern University of Science and Technology (SUSTech), Shenzhen 518055, China*

ARTICLE INFO

ABSTRACT

Exploiting highly efficient oxygen-evolving electrocatalysts is crucial for hydrogen production through seawater electrolysis. Here, a hierarchical structure of boron-doped (Ni,Fe)OOH grown on Ni$_3$N nanosheets supported on nickel foam [denoted as B-(Ni,Fe)OOH/Ni$_3$N/NF] is fabricated. Benefiting from the formation of abundant active sites and the reduced free energy barrier of the rate-determining step caused by B doping, the obtained B-(Ni,Fe) OOH/Ni$_3$N/NF exhibits extraordinary electrocatalytic activity for oxygen evolution reaction, requiring over-potentials of only 283 mV and 309 mV to achieve a current density of 1000 mA cm^{-2} in alkaline pure water and seawater media, respectively, as well as superior stability. When driven by a commercial Si solar cell, the electrolyzer using B-(Ni,Fe)OOH/Ni$_3$N/NF as the anode and a previously reported Ru/(Fe,Ni)(OH)$_2$/NF as the cathode can achieve a high current of over 1000 mA in alkaline seawater media. This shows the great potential in applying a photovoltaic-driven electrolyzer toward large-scale hydrogen production in seawater electrolysis.

1. Introduction

Resolving the global energy crisis and achieving zero-carbon-dioxide emissions require efforts to reduce the use of traditional fossil fuels worldwide [1–3]. Hydrogen has drawn wide attention in the promotion of clean energy due to its renewable nature and its high energy density [4]. Water splitting, consisting of the anodic oxygen evolution reaction (OER) and the cathodic hydrogen evolution reaction (HER), shows great potential for acquiring high-purity hydrogen [5–7]. However, the operation of commercially available water electrolyzers has thus far relied heavily on high-purity freshwater. Freshwater accounts for only about 2.5% of the planet's water resources, which significantly limits the large-scale application of water electrolysis technology, especially in regions where freshwater is in short supply. Success in hydrogen production *via* seawater splitting could significantly reduce the dependence on high-purity freshwater for electrolysis [8]. Additionally, hydrogen generated *via* water electrolysis currently accounts for only 4% of total hydrogen production [9], mainly due to high energy consumption and the scarcity of noble-metal-based electrocatalysts. OER, a four-electron

transfer process, requires efficient catalysts to surmount the high activation energy barrier, especially at industrially required current densities (> 500 mA cm^{-2}) [10,11]. Moreover, the OER process in natural seawater media is more challenging than in freshwater. For instance, the anode of a seawater electrolyzer often suffers from the competition reaction of Cl$^-$ oxidation, the strong corrosive effect of chlorine-based compounds on the electrode, and the burial of active sties caused by the formation of insoluble precipitates such as magnesium hydroxide and calcium hydroxide on the catalyst surface [8,12]. Therefore, it is highly desirable to exploit cost-effective, highly active, and robust OER electrocatalysts to accelerate the development of hydrogen production *via* seawater electrolysis technology.

The Pourbaix diagram indicates that the difference in the onset potential between the OER and the chlorine evolution reaction (ClER) reaches its maximum value of 490 mV in aqueous saline electrolytes (pH > 7.5) [13]. This suggests that seawater electrolysis in alkaline media can reduce the possibility of the ClER occurring in a specific voltage range. Recently, transition-metal oxyhydroxides have received considerable attention due to their high intrinsic activity for catalyzing OER in

---

alkaline media [14–17]. For instance, our previously reported S-doped Ni/Fe (oxy)hydroxide catalyst requires an overpotential as low as about 328 mV to achieve a current density of 500 mA cm^{-2} in alkaline electrolyte, outperforming most other OER catalysts [18]. The outstanding performance of metal oxyhydroxides places them among the top tier of OER electrocatalysts, prevailing over the state-of-the-art ruthenium- and iridium-based oxides. Regrettably, most pure transition-metal oxyhydroxides display undesirable adsorption/desorption strength for OER intermediates, or low conductivity or poor stability in seawater media, which significantly limits their practical applications [10,19]. Meanwhile, some active sites could be buried by the formation of precipitates during the OER process in natural seawater media. Therefore, it would be highly desirable to develop an efficient OER catalyst with moderate adsorption/desorption strength for reaction intermediates, high electrical conductivity, superior chlorine corrosion resistance, and abundant catalytic active sites for seawater splitting.

Two-dimensional (2D) transition-metal compounds grown directly on nickel foam (NF), such as CoP$_x$/NF [12] and Ni$_3$N/NF [20], can form a highly conductive and stable secondary substrate and display strong mechanical stability, thus providing a larger surface area on which to load more active material and serving as an ideal current-collecting substrate to ensure efficient electron transfer to the electrocatalyst it supports, as well as exhibiting excellent resistance to chlorine corrosion in seawater media. Here, an alternating dip-coating method is used to rapidly grow (within 200 s) boron-doped (Ni,Fe)OOH on a self-supporting transition nitride grown on NF [denoted as B-(Ni,Fe) OOH/Ni$_3$N/NF], in which B-(Ni,Fe)OOH and Ni$_3$N/NF serve as the active sites and the secondary substrate, respectively. The fabricated hierarchical B-(Ni,Fe)OOH/Ni$_3$N/NF electrode guarantees efficient electron transport and mass transfer, sufficient chemically stable catalytic sites, and a reduced free energy barrier of the rate-determining step for OER. All these features enable B-(Ni,Fe)OOH/Ni$_3$N/NF to exhibit outstanding electrocatalytic performance for OER. The obtained electrode requires overpotentials of only 283 mV and 309 mV to deliver an extremely high current density of 1000 mA cm^{-2} in alkaline pure water and seawater media, respectively, superior to most previously reported OER catalysts [18,21,22], as well as exhibiting excellent stability under high current density. Furthermore, an electrolyzer consisting of B-(Ni, Fe)OOH/Ni$_3$N/NF (anode) and a previously reported Ru/(Fe,Ni) (OH)$_2$/NF (cathode) [23] driven by a commercial Si solar cell can achieve an impressively high current of 1030 mA for seawater splitting. This work may thus have a practical impact on advancing the carbon-free hydrogen economy through the combination of seawater electrolysis and renewable solar energy.

2. Experimental section

2.1. Materials

Fe(NO$_3$)$_3$·9 H$_2$O (Sigma-Aldrich), FeCl$_3$·6 H$_2$O (Sigma-Aldrich), Ni (NO$_3$)$_2$·6 H$_2$O (Sigma-Aldrich), Co(NO$_3$)$_2$·6 H$_2$O (Sigma-Aldrich), RuCl$_3$ (Sigma-Aldrich), Na$_2$MoO$_4$·2 H$_2$O (Sigma-Aldrich), Mn (CH$_3$COO)$_4$·4 H$_2$O (Sigma-Aldrich), NaBH$_4$ (Sigma-Aldrich), N$_2$H$_4$ (Aladdin), KOH (50% w/v, Alfa Aesar), HCl (36 wt%, Macron Fine Chemicals), NaOH (Sigma-Aldrich), nickel foam (Sigma-Aldrich), Nafion 117 solution (5%, Sigma-Aldrich), NaCl (Fisher Chemical), Pt/C (20%, Johnson Matthey), IrO$_2$ (99%, Alfa Aesar), and ethanol (Decon Labs, Inc.) were used as received. Natural seawater was collected from Galveston Bay, Texas, USA, and impurities visible to the naked eye were filtered out prior to use.

2.2. Preparation of materials

2.2.1. Preparation of Ni(OH)$_2$/NF

A piece of nickel foam (NF, 3 cm × 4 cm) was first cleaned with 3 M HCl, ethanol, and deionized water solution for 15 min each *via*

ultrasonication treatment. Ni(OH)$_2$ nanosheets were *in situ* grown on the NF *via* a dissolution-precipitation mechanism during hydrothermal treatment. In a typical synthesis, 50 μL of 3 M HCl was added into 50 mL of deionized water solution and the as-prepared solution was used to etch the NF surface, resulting in the formation of Ni^{2+} ions in the solution. The cleaned NF was subsequently immersed into the as-obtained solution and transferred into a Teflon-lined stainless-steel autoclave, and then maintained at 160 °C for 8 h in an electric oven. Finally, the Ni (OH)$_2$/NF precursor was washed with deionized water several times.

2.2.2. Preparation of Ni$_3$N/NF

In a typical synthesis, the Ni(OH)$_2$/NF precursor was placed in a tube furnace and then heated to 450 °C at a rate of 5 °C min^{-1} under a flowing NH$_3$ atmosphere (60 standard cubic centimeters per minute, 1 bar) for 2 h. Afterward, the furnace was allowed to naturally cool down to room temperature under NH$_3$ atmosphere. As a result, Ni$_3$N/NF was successfully obtained.

2.2.3. Preparation of B-(Ni,M)OOH/Ni$_3$N/NF (M = Fe, Co, Mo, or Mn), B-NiOOH/Ni$_3$N/NF, and B-FeOOH/Ni$_3$N/NF

To synthesize B-(Ni,Fe)OOH on the surface of Ni$_3$N/NF, a mixed metal salt solution of 0.1 M Ni(NO$_3$)$_2$·6 H$_2$O and 0.05 M Fe(NO$_3$)$_3$·9 H$_2$O (solution A) and a mixed reducing solution of 0.375 M NaBH$_4$ and 0.1 M NaOH (solution B) were each prepared. The obtained Ni$_3$N/NF was immersed into solution A and solution B for 10 s each, and these steps were repeated for 10 cycles. Following the cycles of immersion, the prepared samples were washed with deionized water several times and then dried in air. As a result, B-(Ni,Fe)OOH/Ni$_3$N/NF was obtained. The procedure for preparing B-(Ni,M)OOH (M = Co, Mo, or Mn) on the surface of Ni$_3$N/NF is similar to the synthesis of B-(Ni,Fe)OOH/Ni$_3$N/ NF, except that the 0.05 M Fe(NO$_3$)$_3$·9 H$_2$O in solution A was replaced with 0.05 M Co(NO$_3$)$_2$·6 H$_2$O, 0.05 M Na$_2$MoO$_4$·2 H$_2$O, or 0.05 M Mn (CH$_3$COO)$_4$·4 H$_2$O, respectively. Additionally, B-NiOOH/Ni$_3$N/NF and B-FeOOH/Ni$_3$N/NF were also prepared, in which 0.15 M Ni (NO$_3$)$_2$·6 H$_2$O and 0.15 M Fe(NO$_3$)$_3$·9 H$_2$O, respectively, were used as the metal salt solution (solution A).

2.2.4. Preparation of (Ni,Fe)OOH/Ni$_3$N/NF

The synthesis of (Ni,Fe)OOH/Ni$_3$N/NF was the same as that for B-(Ni,Fe)OOH/Ni$_3$N/NF except that no NaBH$_4$ was added in solution B.

2.2.5. Preparation of R-(Ni,Fe)OOH/Ni$_3$N/NF

The synthesis of R-(Ni,Fe)OOH/Ni$_3$N/NF was the same as that for B-(Ni,Fe)OOH/Ni$_3$N/NF except that NaBH$_4$ in solution B was replaced with N$_2$H$_4$.

2.2.6. Preparation of B-(Ni,Fe)OOH/NF and B-(Ni,Fe)OOH/Ni(OH)$_2$/NF

The synthesis of B-(Ni,Fe)OOH/NF and B-(Ni,Fe)OOH/Ni(OH)$_2$/NF was the same as that for B-(Ni,Fe)OOH/Ni$_3$N/NF except that Ni$_3$N/NF was replaced by pure NF and Ni(OH)$_2$/NF, respectively.

2.2.7. Preparation of B-(Ni,Fe)OOH-Ni$_3$N/NF

B-(Ni,Fe)OOH powder was prepared using a process similar to that for synthesizing B-(Ni,Fe)OOH on the surface of Ni$_3$N/NF. In a typical synthesis, a mixed solution of 0.1 M Ni(NO$_3$)$_2$·6 H$_2$O and 0.05 M Fe (NO$_3$)$_3$·9 H$_2$O was gradually added into a mixed solution of 0.375 M NaBH$_4$ and 0.1 M NaOH. The resulting precipitate was centrifuged and washed several times, and then dried in air to obtain B-(Ni,Fe)OOH powder. Afterward, the B-(Ni,Fe)OOH powder was dispersed on the surface of Ni$_3$N/NF to obtain the B-(Ni,Fe)OOH-Ni$_3$N/NF electrode.

2.2.8. Preparation of Ru/(Fe,Ni)(OH)$_2$/NF

The synthesis procedure for Ru/(Fe,Ni)(OH)$_2$/NF was exactly the same as in our previous work [23]. In a typical synthesis, 16 mg of FeCl$_3$·6 H$_2$O and 50 μL of 3 M HCl were dissolved into 50 mL of deionized water under vigorous stirring. Afterward, the mixture was

transferred to a Teflon-lined stainless-steel autoclave with a piece of cleaned NF and maintained at 160 °C for 8 h, and then the (Fe,Ni) $(OH)_2$/NF precursor was obtained. Finally, the (Fe,Ni)$(OH)_2$/NF was immersed in 4 mg mL^{-1} RuCl$_3$ solution for 10 h and then washed with deionized water to obtain Ru/(Fe,Ni)$(OH)_2$/NF.

2.2.9. Preparation of IrO$_2$/NF and Pt/C/NF

2 mg of IrO$_2$ or Pt/C powder was dispersed into 1 mL of a mixed solution containing 0.2 mL of water, 0.77 mL of ethanol, and 0.03 mL of Nafion. The obtained catalyst liquid was then drop-dried onto the NF to obtain IrO$_2$/NF and Pt/C/NF, respectively.

2.3. Material characterization

Scanning electron microscopy (SEM, LEO 1525) and transmission electron microscopy (TEM, JEOL 2010 F) were carried out to characterize the morphology and lattice fringes, respectively, of the prepared materials. Energy-dispersive X-ray spectroscopy (EDX) analysis was performed using scanning transmission electron microscopy (STEM). X-ray diffraction (XRD, PANalytical X'Pert Pro) and X-ray photoelectron spectroscopy (XPS, PHI Quantera) measurements were used to characterize the crystal phase and chemical binding states, respectively, of the prepared materials. The binding energy calibration uses the C 1 s peak at 284.8 eV as a reference.

2.4. Electrochemical measurement

The evaluation of electrochemical activity for all as-prepared materials was carried out on an electrochemical workstation (Gamry Framework, U.S.) with a three-electrode electrochemical cell system, in which an obtained electrocatalyst, Hg/HgO, and a carbon rod were used as the work electrode, the reference electrode, and the auxiliary electrode, respectively. The electrochemical measurements of the catalysts were performed in 1 M KOH, 1 M KOH + x M NaCl (x = 0.5, 1, 2, or 5), or 1 M KOH + natural seawater. All potentials were calibrated to reversible hydrogen electrode (RHE). All polarization curves were recorded *via* linear sweep voltammetry (LSV) measurements at a scanning rate of 5 mV s^{-1} and were recorded with and without *iR* compensation. The geometrical area of the electrode was used to normalize the current density.

2.5. O$_2$ evolution rate analysis

Faradaic efficiency (FE) testing was performed for B-(Ni,Fe)OOH/Ni$_3$N/NF. The O$_2$ evolution rate was calculated using the equation $v = n/t$, in which v is the O$_2$ evolution rate, n is the amount of O$_2$ (mol), and t is the time (s). Here we take the current density of 100 mA cm^{-2}, electrode area of 1 cm^2, and time of 3600 s as an example to illustrate the actual rate of O$_2$ production:

$n = 97\% \times (0.1 \text{ A cm}^{-2} \times 1 \text{ cm}^2 \times 3600 \text{ s})/(4 \times 96485 \text{ C mol}^{-1}) = 9.048 \times 10^{-4}$ mol.

$v = n/t = 2.51 \times 10^{-7}$ mol s^{-1}.

Therefore, the actual rate of O$_2$ production at a current density of 100 mA cm^{-2} is 2.51×10^{-7} mol s^{-1}.

2.6. Detection of hypochlorite

After completing OER testing at a fixed current density of 100 mA cm^{-2} for 0.5 h in alkaline seawater media, the presence of hypochlorite in the electrolyte was determined using a chlorine (hypochlorite) visual test kit (details shown at https://www.chemetrics.com/product/k-5808). The color of the solution in the tube will change to pink if the tested sample contains hypochlorite due to the detection mechanism. The more intense the color of the solution in the tube, the higher the hypochlorite content in the tested sample.

2.7. DFT calculation details

Density functional theory (DFT) calculations were performed using Vienna Ab-initio Simulation Package (VASP) within the generalized gradient approximation (GGA) of the Perdew-Burke-Ernzerhof (PBE) functional [24,25]. The projector augmented wave (PAW) method was employed to calculate the core-valence electron interaction [26] and the plane-wave basis set was used with a cutoff energy of 550 eV. Partial occupancies of the Kohn-Sham orbitals were allowed using the Gaussian smearing method and a width of 0.05 eV. The DFT + U method was applied to better describe the core states for transition metals. The vacuum layer of 16 Å between periodically repeated slabs was set to avoid interactions among slabs. The $2 \times 2 \times 1$ Monkhorst-Pack k-point grid was chosen for slab calculations. A supercell with 32 H atoms, 64 O atoms, 16 Fe atoms, and 16 Ni atoms was used to model the (Ni,Fe)OOH material. The model for B-(Ni,Fe)OOH was also constructed *via* partially replacing surface oxygen atoms with B atoms.

The free energy was corrected at the temperature of 298.15 K. Accordingly, the free energy formula can be expressed as follows.

$$\Delta G = \Delta E_{DFT} + \Delta ZPE - T\Delta S$$

where ΔE_{DFT}, ΔZPE, and ΔS represent the total energy based on the DFT calculations, zero-point energy, and entropy corrections, respectively.

3. Results and discussion

3.1. Catalyst synthesis and physical characterizations

Scheme 1 illustrates the synthesis of B-(Ni,Fe)OOH/Ni$_3$N/NF. Briefly, Ni$(OH)_2$ nanosheets were *in situ* grown on a NF substrate through a dissolution-precipitation mechanism during hydrothermal treatment, in which the NF not only served as the high-conductivity substrate but also as the source of Ni for the growth of Ni$(OH)_2$. Afterward, the Ni$(OH)_2$ was successfully converted to highly conductive Ni$_3$N through a nitridation process. An ultra-fast chemical reduction method, requiring only 200 s to complete, was employed at room temperature to fabricate the highly active component B-(Ni,Fe)OOH on the Ni$_3$N/NF. The compound obtained using this method is a metal oxyhydroxide rather than an alloy, possibly due to the rapid hydrolysis of alloy borides in alkaline solution at room temperature [27]. The entire process is energy-saving and facile for fabricating electrocatalysts with large surface areas, and it can be scaled up for industrial application. Furthermore, the *in situ* growth of the highly active catalyst on the large surface area of the highly conductive Ni$_3$N was found to be beneficial to provide a large number of active sites and enhance the electrode stability during electrochemical testing. Scanning electronic microscopy (SEM) images in Fig. 1a-c show that the morphology of the material changes with the growth of different active layers. Ni$_3$N nanosheets were uniformly distributed on the conductive NF substrate (Fig. 1b). After a further treatment in which the Ni$_3$N/NF was alternately and repeatedly dipped into a metal-salt solution and a NaBH$_4$ solution, the surfaces of the Ni$_3$N nanosheets became covered with the particle-structured B-(Ni,Fe)OOH (Fig. 1c). The presence of some lattice fringes of B-(Ni,Fe)OOH/Ni$_3$N/NF was confirmed by high-resolution transmission electronic microscopy (HRTEM). The HRTEM images in Fig. S1a and S1b show distinguishable crystal planes with spacings of 0.231 and 0.204 nm, which correspond to the (110) and (111) planes of Ni$_3$N, respectively. Meanwhile, the HRTEM image in Fig. 1d shows two interleaved crystal planes with inter-plane spacings of 0.208 and 0.214 nm and an intersection angle of about 50.2°, which further confirms the existence of NiOOH (JCPDS No. 27–0956) [28]. In the HRTEM image in Fig. 1e, two interleaved crystal planes with inter-plane spacings of 0.221 and 0.247 nm and an intersection angle of about 56° confirm the formation of FeOOH (JCPDS No. 26–0792) [29]. Additionally, elemental mapping of B-(Ni,Fe)OOH/-Ni$_3$N/NF was conducted *via* energy-dispersive X-ray spectroscopy (EDX)
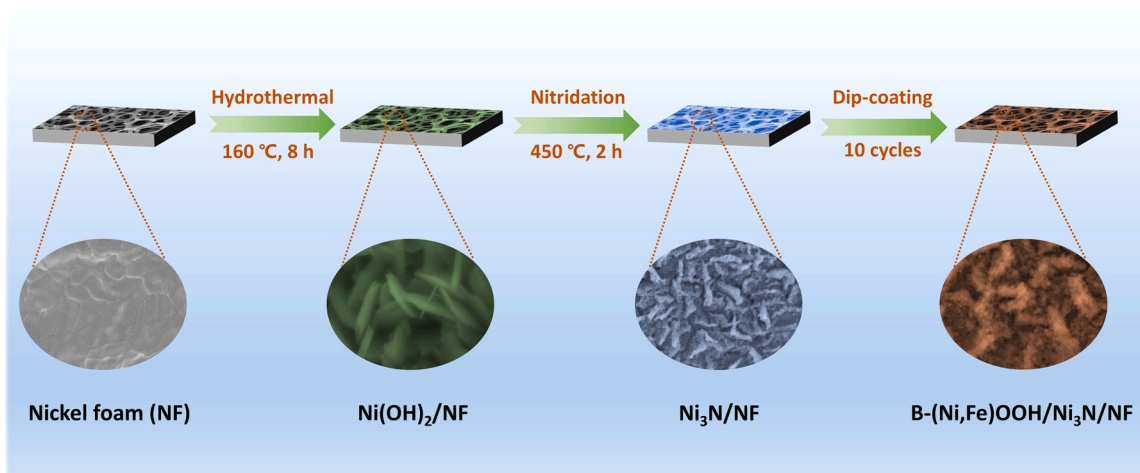
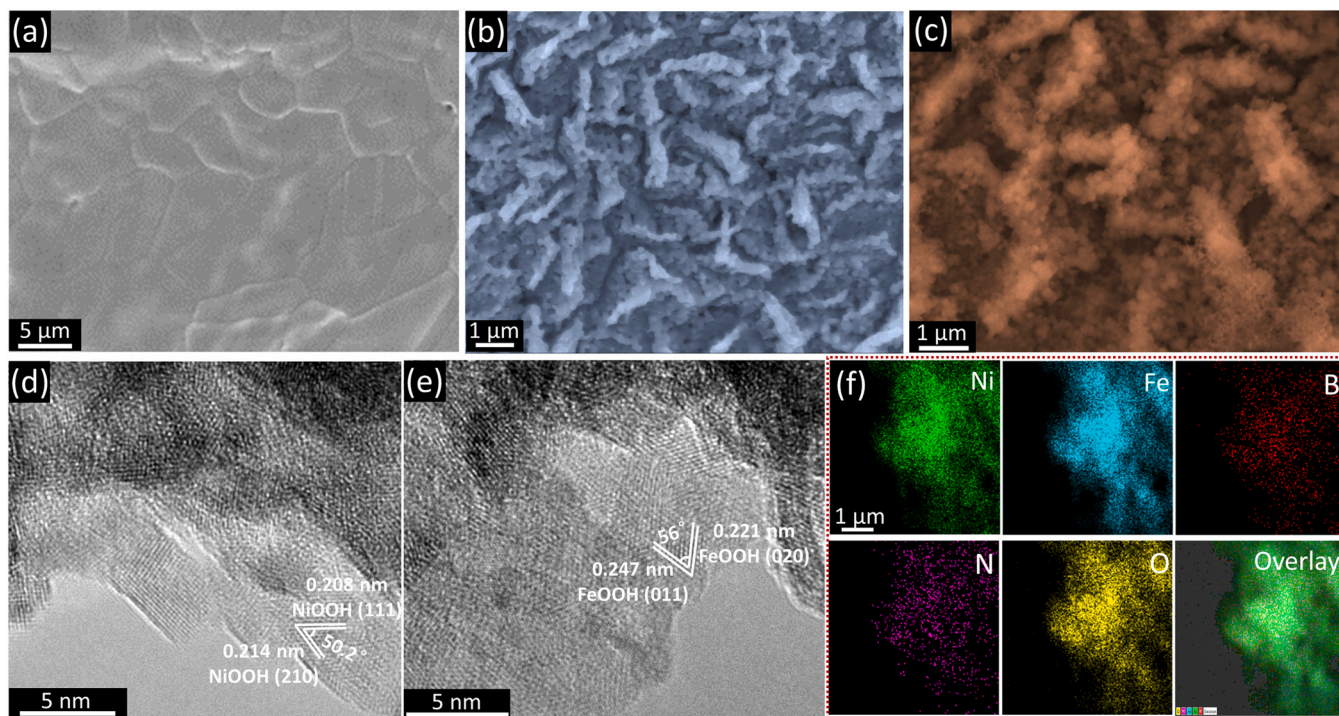**Scheme 1.** Schematic representation of the formation of B-(Ni,Fe)OOH/Ni$_3$N/NF.

Fig. 1. SEM images of (a) pure nickel foam, (b) Ni$_3$N, and (c) B-(Ni,Fe)OOH/Ni$_3$N/NF. (d) and (e) HRTEM images of B-(Ni,Fe)OOH/Ni$_3$N/NF. (f) EDX STEM elemental mapping images of B-(Ni,Fe)OOH/Ni$_3$N/NF.

performed using scanning transmission electron microscopy (STEM), and the results shown in Fig. 1f reveal the homogeneous distribution of elemental Ni, Fe, B, N, and O throughout the sample.

The crystal structure of the prepared materials was further confirmed by XRD pattern characterization. As shown in Fig. 2a, for both B-(Ni,Fe) OOH/Ni$_3$N/NF and Ni$_3$N/NF, the XRD peaks at 44.5°, 51.8°, and 76.4° correspond to cubic Ni (JCPDS No. 04–0850) [30] and all other peaks are well assigned to hexagonal Ni$_3$N (JCPDS No. 10–0280) [31]. Peaks corresponding to some crystal planes of Ni$_3$N detected during HRTEM characterization, such as the (110) and (111) planes, also appeared in the XRD patterns, which further confirms the existence of Ni$_3$N. The failure to observe any signal for B-(Ni,Fe)OOH may be due to its low crystallinity or its scarcity, either of which would make it difficult to be detected by XRD. However, the presence of NiOOH and FeOOH phases was confirmed by HRTEM characterization since HRTEM has higher

resolution for structural characterization in comparison with XRD. Fig. 2b shows the high-resolution X-ray photoelectron spectroscopy (XPS) spectrum of Ni 2p for B-(Ni,Fe)OOH/Ni$_3$N/NF. The peak at a binding energy of about 856 eV represents the characteristic Ni 2p$_{3/2}$ of Ni^{3+}, which matches well the characteristic peak for NiOOH [32]. Similarly, peaks for Fe^{3+} were observed in the high-resolution XPS spectrum of Fe 2p, as shown in Fig. 2c, and are located at binding energy values of about 711.1 eV and 724.7 eV, which match well with the characteristic peak for FeOOH [33]. Correspondingly, the bond between B and Ni/Fe was detected in the high-resolution XPS spectrum of B 1 s, and is located at a binding energy of about 187.4 eV (Fig. 2d) [34]. The peak at a binding energy of 191.5 eV is attributed to the oxidized boron resulting from exposure to air [35]. Fig. 2e shows the deconvolution of O 1 s, in which the typical peaks at binding energies of about 529.7 and 531.2 eV are indexed to the oxygen in metal oxides (M-O) and hydroxyl
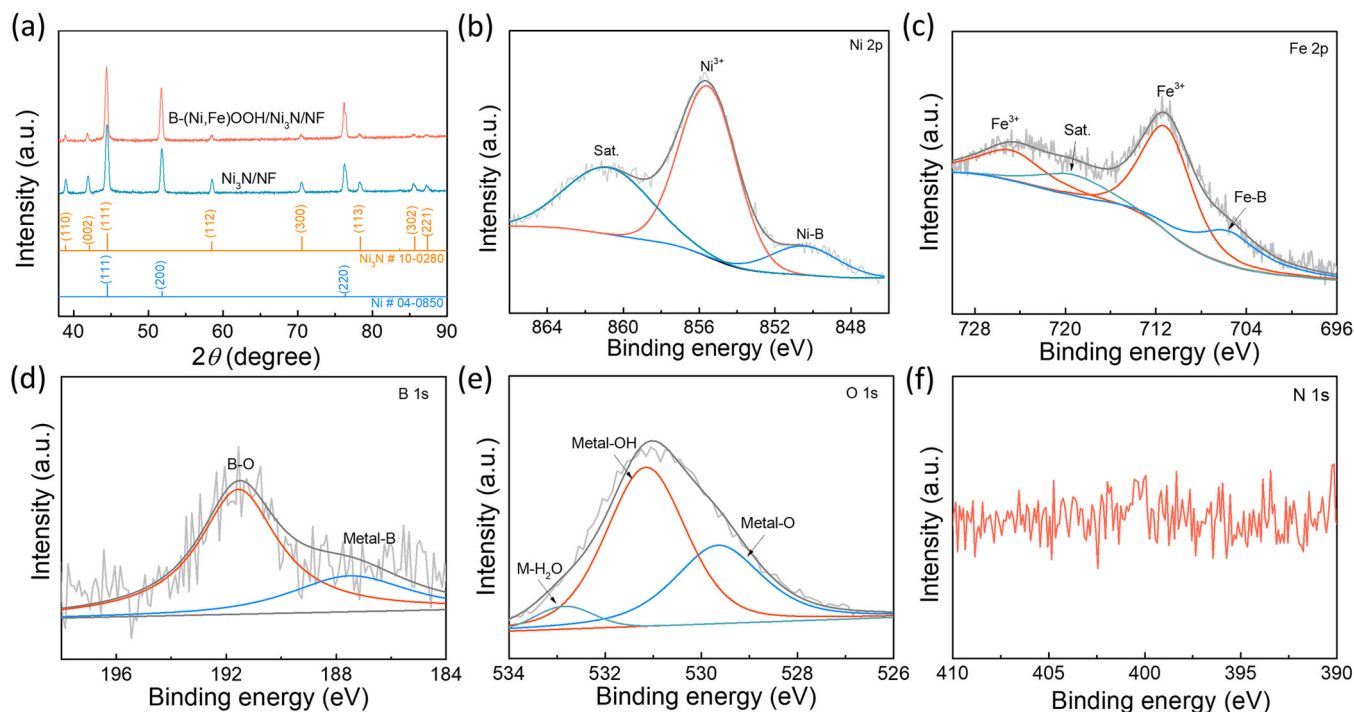
Fig. 2. (a) XRD patterns of the as-prepared materials. High-resolution XPS spectra of (b) Ni 2p, (c) Fe 2p, (d) B 1 s, (e) O 1 s, and (f) N 1 s for B-(Ni,Fe)OOH/Ni$_3$N/NF.

(M-OH), respectively [36]. Therefore, the above-mentioned XPS results further demonstrate the existence of the highly active components NiOOH and FeOOH in B-(Ni,Fe)OOH/Ni$_3$N/NF. As for the high-resolution XPS spectrum of N 1 s shown in Fig. 2 f, no obvious characteristic peak was observed, presumably due to the coverage of Ni$_3$N by B-(Ni,Fe)OOH. It should be noted that the failure to observe Ni^0 from Ni and Ni$^+$ or N from Ni$_3$N is mainly due to XPS being a highly sensitive surface analysis method that probes only about the top 10 nm

of a material. Additionally, the binding energies of Ni 2p and Fe 2p for B-(Ni,Fe)OOH/Ni$_3$N/NF were found to be slightly lower than those for (Ni,Fe)OOH/Ni$_3$N/NF (Figs. S2a and 2b), which is likely due to the use of reductive NaBH$_4$ during the preparation process for the former, resulting in partial reduction of the metal species.
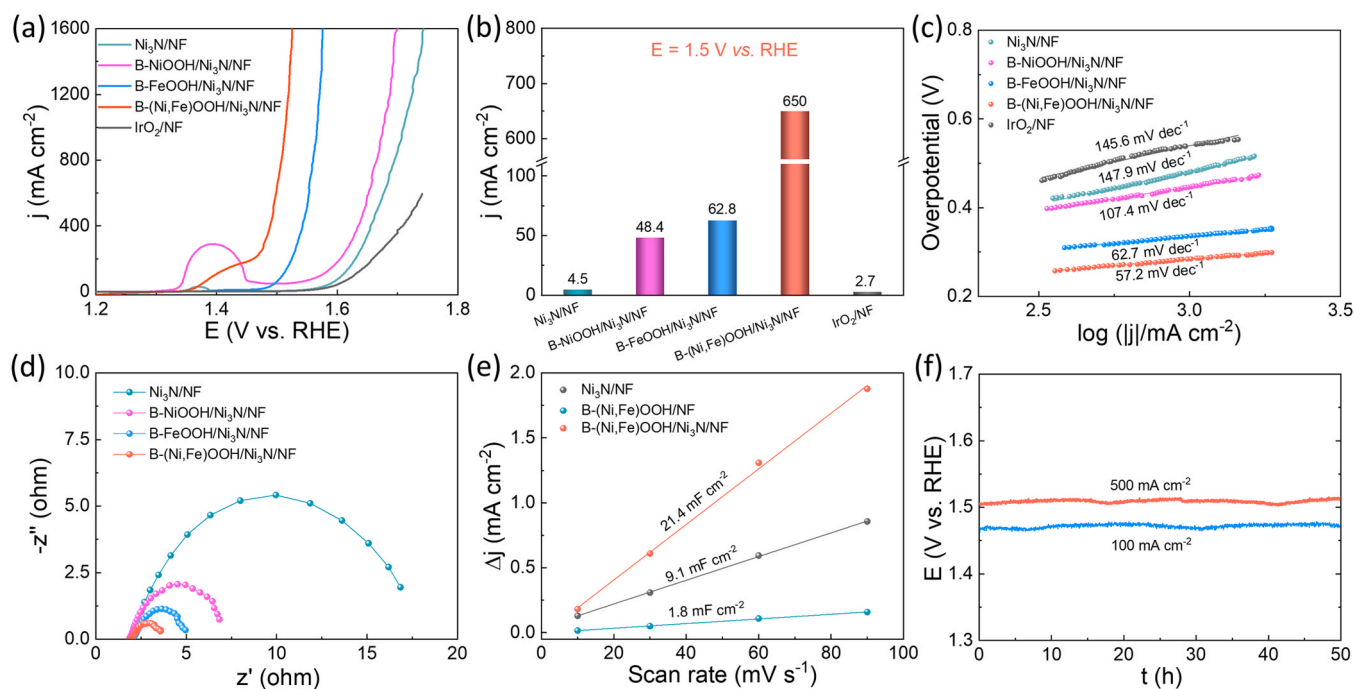

Fig. 3. (a) OER polarization curves, (b) current densities at a potential of 1.5 V *vs.* RHE, (c) corresponding Tafel plots, (d) EIS Nyquist plots, and (e) calculated C$_{dl}$ values of the as-prepared materials in 1 M KOH solution. (f) Long-term stability testing of the B-(Ni,Fe)OOH/Ni$_3$N/NF electrode at constant current densities of 100 mA cm^{-2} and 500 mA cm^{-2} in 1 M KOH solution.

3.2. Electrocatalytic property measurements

The electrocatalytic behavior of the as-prepared materials toward OER was evaluated using a traditional three-electrode cell. It should be noted that the reading of the current density value for the B-(Ni,Fe) OOH/Ni₃N/NF electrode is determined from the reverse cyclic voltammetry (CV) curve since there is a strong oxidation peak in the forward scan (Fig. S3). The obtained B-(Ni,Fe)OOH/Ni₃N/NF electrode requires an overpotential of only 240 mV to achieve a current density of 100 mA cm^{-2} in 1 M KOH solution, which is significantly lower than that for the benchmark IrO₂/NF (398 mV) and for the B-NiOOH/Ni₃N/ NF (343 mV), B-FeOOH/Ni₃N/NF (280 mV), and Ni₃N/NF (378 mV) electrodes under the same current density (Fig. 3a). The polarization curve of the B-(Ni,Fe)OOH/Ni₃N/NF without *iR* compensation is shown in Fig. S4. It is worth mentioning that the OER performance of the (Ni, Fe)OOH/Ni₃N/NF electrode was significantly enhanced with the elemental B doping. As shown in Fig. S5, the B-(Ni,Fe)OOH/Ni₃N/NF electrode requires a much lower overpotential (264 mV) than either (Ni, Fe)OOH/Ni₃N/NF (339 mV) or R-(Ni,Fe)OOH/Ni₃N/NF (307 mV) to reach a current density of 500 mA cm^{-2}. The Faradaic efficiency (FE) for B-(Ni,Fe)OOH-Ni₃N/NF was calculated to be about 97% (Fig. S6). Therefore, the actual rate of O₂ production for the B-(Ni,Fe)OOH/Ni₃N/ NF electrode at a current density of 100 mA cm^{-2} is 2.51×10^{-7} mol s^{-1} (details provided in the Supplementary Material). Additionally, B-(Ni, Fe)OOH/Ni₃N/NF shows excellent electrochemical activity for OER at commercially required current densities. The overpotential needed for B-(Ni,Fe)OOH/Ni₃N/NF to deliver a current density of 500 mA cm^{-2} in 1 M KOH is as low as 264 mV, significantly outperforming the IrO₂/NF electrode (490 mV). Furthermore, this electrode requires an overpotential of only 247 mV to achieve a current density of 1000 mA cm^{-2} under industrial electrolysis conditions at 70 ℃ (Fig. S7), suggesting its broad potential for practical application at such a low overpotential. Fig. 3b displays the current density values achieved at a potential of 1.5 V *vs.* RHE by the prepared materials. Clearly, a current density of 650 mA cm^{-2} achieved by the B-(Ni,Fe)OOH/Ni₃N/NF electrode is far higher than that of the other electrodes under the same condition, suggesting its outstanding electrocatalytic activity for OER. The performance of the B-(Ni,Fe)OOH/Ni₃N/NF electrode is also superior to other reported OER electrocatalysts (Table S1), such as S-doped Ni/Fe (oxy)hydroxide (60 mA cm^{-2} at 1.5 V) [18] and iron/vanadium co-doped nickel (oxy)hydroxide (130 mA cm^{-2} at 1.5 V) [37]. The OER performance of the electrode prepared by dispersing B-(Ni,Fe)OOH powder onto the Ni₃N/NF [denoted as B-(Ni,Fe)OOH-Ni₃N/NF] is clearly inferior to that of the *in situ* grown sample (Fig. S8a), indicating that the *in situ* growth of highly active material on the self-supporting substrate plays a significant role in improving the activity of the entire electrode. The conductivity of Ni₃N also plays a critical role in enhancing the OER activity of B-(Ni,Fe)OOH/Ni₃N/NF. The B-(Ni,Fe) OOH/Ni(OH)₂/NF electrode exhibits worse OER activity than B-(Ni,Fe) OOH/Ni₃N/NF (Fig. S8b), which is mainly due to the low conductivity of Ni(OH)₂ and thus the limited electron transfer ability during the OER process [38]. Furthermore, the OER activity of the electrode for B-(Ni, Fe)OOH deposited on the pure NF is inferior to that on Ni₃N/NF, which may be attributed to the large surface area of Ni₃N/NF for loading active components, enabling the catalyst to exhibit a greater number of exposed active sites. The above discussion indicates that both the conductivity and the surface area of the substrate are vital to the activity of the catalyst. The activity of B-(Ni,M)OOH/Ni₃N/NF (M = Co, Mo, or Mn) was also investigated (Fig. S9). B-(Ni,Fe)OOH/Ni₃N/NF exhibits much better OER activity than B-(Ni,Co)OOH/Ni₃N/NF, B-(Ni,Mo) OOH/Ni₃N/NF, or B-(Ni,Mn)OOH/Ni₃N/NF, indicating that the electrode with a combination of Ni and Fe delivers higher catalytic activity for OER than those with other components. The synergistic effect between the Ni and Fe species, in which the Ni species acts as an intermediate for the formation of active O radicals and the Fe species effectively catalyzes the subsequent O-O coupling [39,40], contributes

to the optimal OER performance of B-(Ni,Fe)OOH/Ni₃N/NF.

The Tafel slope values of the as-prepared electrodes were determined to further understand the mechanism for the enhanced OER activity of B-(Ni,Fe)OOH/Ni₃N/NF. As shown in Fig. 3c, B-(Ni,Fe)OOH/Ni₃N/NF exhibits a much smaller Tafel slope value (57.2 mV dec^{-1}) than B-NiOOH/Ni₃N/NF (107.4 mV dec^{-1}), B-FeOOH/Ni₃N/NF (62.7 mV dec^{-1}), Ni₃N/NF (147.9 mV dec^{-1}), and even IrO₂/NF (145.6 mV dec^{-1}), indicating the more favorable reaction kinetics on the B-(Ni,Fe) OOH/Ni₃N/NF electrode. Moreover, the electrochemical impedance spectroscopy (EIS) results shown in Fig. 3d indicate that the B-(Ni,Fe) OOH/Ni₃N/NF electrode exhibits the smallest Nyquist semicircle diameter. This suggests that it has higher electrical conductivity and a more favorable charge transfer ability during the OER process compared to the other materials studied. Electrochemical surface area (ECSA) was also determined according to the CV curves obtained at different scanning rates (Fig. S10). As shown in Fig. 3e, B-(Ni,Fe)OOH/Ni₃N/NF displays the largest electrochemical double layer capacitance (C$_{dl}$) value (21.4 mF cm^{-2}) among the investigated samples, nearly 12 times as high as that of B-(Ni,Fe)OOH/NF (1.8 mF cm^{-2}). This suggests that the entire surface of each Ni₃N nanosheet is beneficial in providing a larger surface area to support the B-(Ni,Fe)OOH, thus significantly increasing the number of active sites exposed to electrolyte for the B-(Ni,Fe)OOH/ Ni₃N/NF electrode. Hydrophilicity plays a vital role in OER, especially at an extremely high current density. This feature directly influences the contact between the electrolyte and the active sites. Therefore, the wetting contact angle between the electrolyte and the electrode was measured. Clearly, the hydrophilicity of the electrode is significantly improved after the formation of B-(Ni,Fe)OOH/Ni₃N on the NF substrate surface (Fig. S11). Therefore, the contact between the electrolyte and the catalytic active sites is significantly enhanced, which correspondingly promotes the formation of oxygen gas on the B-(Ni,Fe)OOH/Ni₃N/ NF electrode.

The stability of an electrode directly determines its potential for application in industry, especially at high current density. Thus, we performed chronopotentiometry measurements on the B-(Ni,Fe)OOH/ Ni₃N/NF electrode at current densities of 100 mA cm^{-2} and 500 mA cm^{-2}. As shown in Fig. 3f, even at a current density as high as 500 mA cm^{-2}, there is no obvious change in the applied potential for B-(Ni,Fe)OOH/Ni₃N/NF throughout 50 h of continuous electrolysis, attesting to the excellent stability of this electrode under high current density. We further performed XRD, SEM, and XPS characterizations on B-(Ni,Fe)OOH/Ni₃N/NF after the long-term stability testing to determine any change in the structure of the electrode. The XRD patterns shown in Fig. S12 indicate that, after long-term stability testing, the B-(Ni,Fe)OOH/Ni₃N/NF electrode still shows the characteristic peaks of Ni₃N and no other peaks appear, meaning that the surface reconstruction may occur on the top layer of the catalyst that cannot show any peaks in XRD. This result further reveals that Ni₃N can maintain a certain level of structural stability during testing. The SEM images shown in Fig. S13 verify that the surface morphology of the B-(Ni,Fe) OOH/Ni₃N/NF electrode was well maintained after long-term stability testing, further demonstrating the strong adhesion between the catalyst and the substrate. The obtained high-resolution XPS spectra displayed in Fig. S14 show that the surface structure of the electrode was well preserved after long-term stability testing, except that the signal for the B-metal bond weakened slightly. This is mainly due to the oxidation of the electrode under high OER potential.

Encouraged by its exceptional catalytic activity and stability in KOH solution, we further evaluated the electrochemical behavior of B-(Ni,Fe) OOH/Ni₃N/NF in simulated and natural seawater. Fig. S15 shows the OER performance of the B-(Ni,Fe)OOH/Ni₃N/NF electrode in different electrolytes. The OER activity of the electrode decreases slightly with increasing NaCl concentration in KOH solution, which may be due to the reduced mass transfer capability caused by the larger amount of Cl⁻ ions in the solution [8]. The B-(Ni,Fe)OOH/Ni₃N/NF electrode also shows outstanding catalytic activity for OER in alkaline natural seawater (1 M

KOH + seawater), requiring an overpotential of only 309 mV to achieve a current density of 1000 mA cm^{-2} (Fig. 4a). This performance is superior to that of most reported OER catalysts in alkaline natural seawater at such a high current density, such as S-(Ni,Fe)OOH (462 mV) [18], NiFe/NiS$_x$-Ni (~ 360 mV) [19], and B-Co$_2$Fe LDH (415 mV) [41]. Additionally, the applied potential needed by B-(Ni,Fe)OOH/Ni$_3$N/NF to reach such a high current density for OER is much lower than the required thermodynamic potential for the oxidation reaction involving Cl$^-$ ions in strong alkaline media, suggesting that the oxidation of Cl$^-$ ions can be effectively avoided, in turn avoiding the corrosion caused by the formation of chloride oxidation products on the electrode. We performed OER testing at a fixed current density of 100 mA cm^{-2} in alkaline natural seawater for about 0.5 h and no hypochlorite was detected in the electrolyte (Fig. S16), further confirming the absence of any oxidation reaction involving Cl$^-$ ions on the anode. Nevertheless, the OER activity of the B-(Ni,Fe)OOH/Ni$_3$N/NF electrode is slightly lower in alkaline natural seawater than in alkaline simulated seawater (1 M KOH + 0.5 M NaCl), which may be caused by its active sites being blocked due to the presence of a large amount of impurities in natural seawater. The EDX spectrum displayed in Fig. S17 shows that elemental Ca, Mg, Na, K, Cl, and S were detected in the electrode after testing in natural seawater. All the newly emerged elements came from the seawater.

Considering the excellent performance of B-(Ni,Fe)OOH/Ni$_3$N/NF in seawater media, we combined it with a HER electrode to fabricate a two-electrode electrolyzer for overall water splitting in alkaline seawater media. Our previously reported Ru/(Ni,Fe)(OH)/NF was selected as the HER catalyst since it exhibits outstanding electrocatalytic activity for HER in both 1 M KOH and 1 M KOH + seawater media (Fig. 4b). As shown in Figs. 4c and 4d, the combined electrolyzer employing B-(Ni,Fe)OOH/Ni$_3$N/NF and Ru/(Ni,Fe)(OH)/NF as the anode and cathode, respectively, delivers a current density of 500 mA cm^{-2} at 1.68 V in alkaline seawater media, performing even better than the benchmark IrO$_2$||Pt/C electrolyzer. Impressively, the combined electrolyzer incorporating our prepared catalysts shows remarkable stability at current densities of 100 and 500 mA cm^{-2}, and no obvious fluctuation was observed even after 50 h of continuous electrolysis under such high

current densities (Fig. 4e). Finally, a commercial Si solar cell (Renogy Corp.) was employed as the power source to drive the combined electrolyzer for water splitting. The solar cell exhibited an output current of 1100 mA and a photovoltage of 5.07 V under simulated sunlight (Figs. S18a and S18b, respectively). The current output for the entire assembled system reached an impressive 1030 mA under a photovoltage of 3.77 V (Fig. 4f, Fig. S19, and Movie S1), demonstrating the great potential for industrial application of hydrogen production through seawater splitting at high current density *via* the combination of a water electrolysis cell and a commercial solar cell.

3.3. DFT analysis

DFT calculations were further performed to gain atomic-scale insights for explaining the role of B doping in enhancing OER activity. It should be noted that the true active sites of B-(Ni,Fe)OOH/Ni$_3$N and (Ni,Fe)OOH/Ni$_3$N were determined to be surface B-(Ni,Fe)OOH and (Ni,Fe)OOH, respectively. Therefore, the active species of (Ni,Fe)OOH and B-(Ni,Fe)OOH were constructed as structure models, and the adsorbate evolution mechanism (AEM) was adopted for OER in the DFT calculations. The optimized theoretical models of the (Ni,Fe)OOH and B-(Ni,Fe)OOH active species are presented in Figs. 5a and 5b, respectively. The free energy diagrams for both active species at a potential of 1.23 V are shown in Fig. 5c. It can be observed that the formation energy of the *OH species for the (Ni,Fe)OOH model is significantly smaller than that for B-(Ni,Fe)OOH, which indicates that it is more difficult to generate *O [42]. As a result, the energy barrier of the rate-determining step (*OH → *O) is 1.72 eV for (Ni,Fe)OOH. After the introduction of B, the formation energy of *O for B-(Ni,Fe)OOH is reduced to 1.46 eV, which indicates the critical role of B doping in improving the OER activity of the B-(Ni,Fe)OOH/Ni$_3$N catalyst. Finally, the theoretical OER overpotentials for the B-(Ni,Fe)OOH and (Ni,Fe)OOH models (0.23 and 0.49 V, respectively) were determined (Fig. 5d), and the results are consistent with the overpotential trend experimentally determined based on the measured LSV curves.
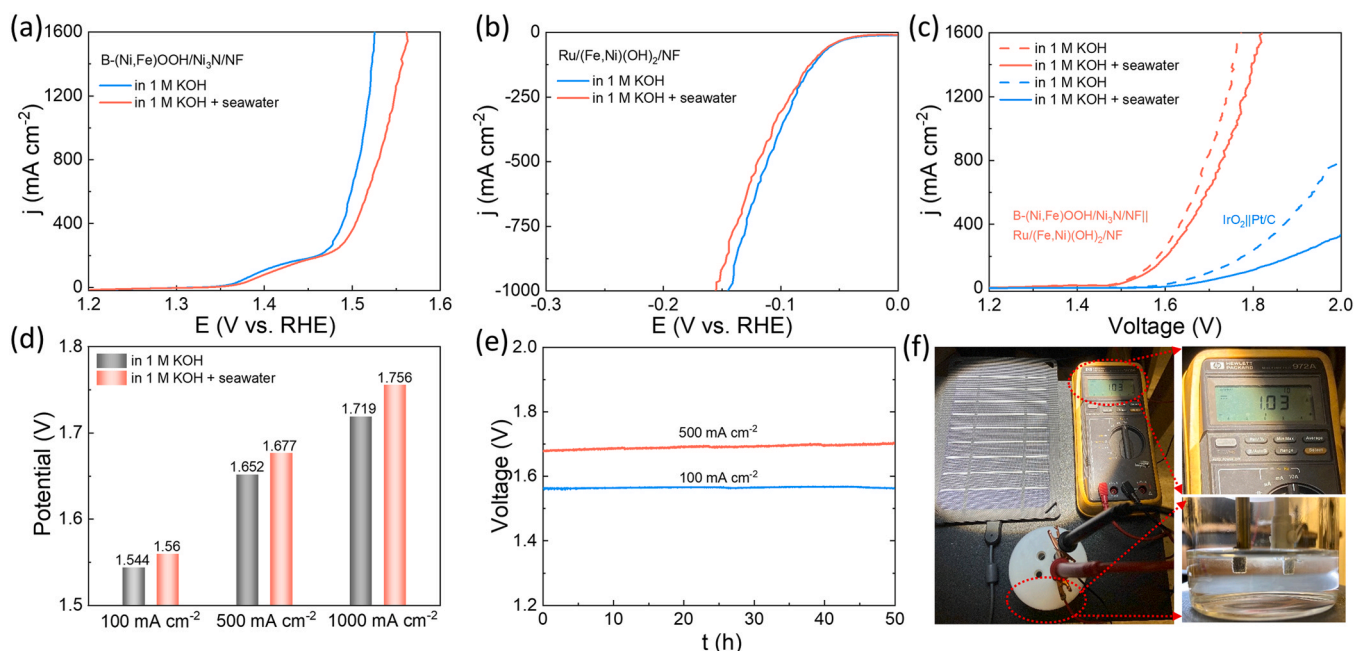

Fig. 4. (a) Polarization curves of B-(Ni,Fe)OOH/Ni$_3$N/NF electrode for OER in different electrolytes. (b) Polarization curves of Ru/(Fe,Ni)(OH)$_2$/NF electrode for HER in different electrolytes. (c) Comparison of the overall water-splitting activity of different electrolyzers in different electrolytes. (d) Required voltages at current densities of 100, 500, and 1000 mA cm^{-2} for the B-(Ni,Fe)OOH/Ni$_3$N/NF||Ru/(Fe,Ni)(OH)$_2$/NF electrolyzer in different electrolytes. (e) Long-term stability testing of the B-(Ni,Fe)OOH/Ni$_3$N/NF||Ru/(Fe,Ni)(OH)$_2$/NF electrolyzer conducted at constant current densities of 100 and 500 mA cm^{-2} in alkaline seawater solution. (f) Seawater splitting using the B-(Ni,Fe)OOH/Ni$_3$N/NF||Ru/(Fe,Ni)(OH)$_2$/NF electrolyzer driven by a commercial Si solar cell at a current of 1030 mA.
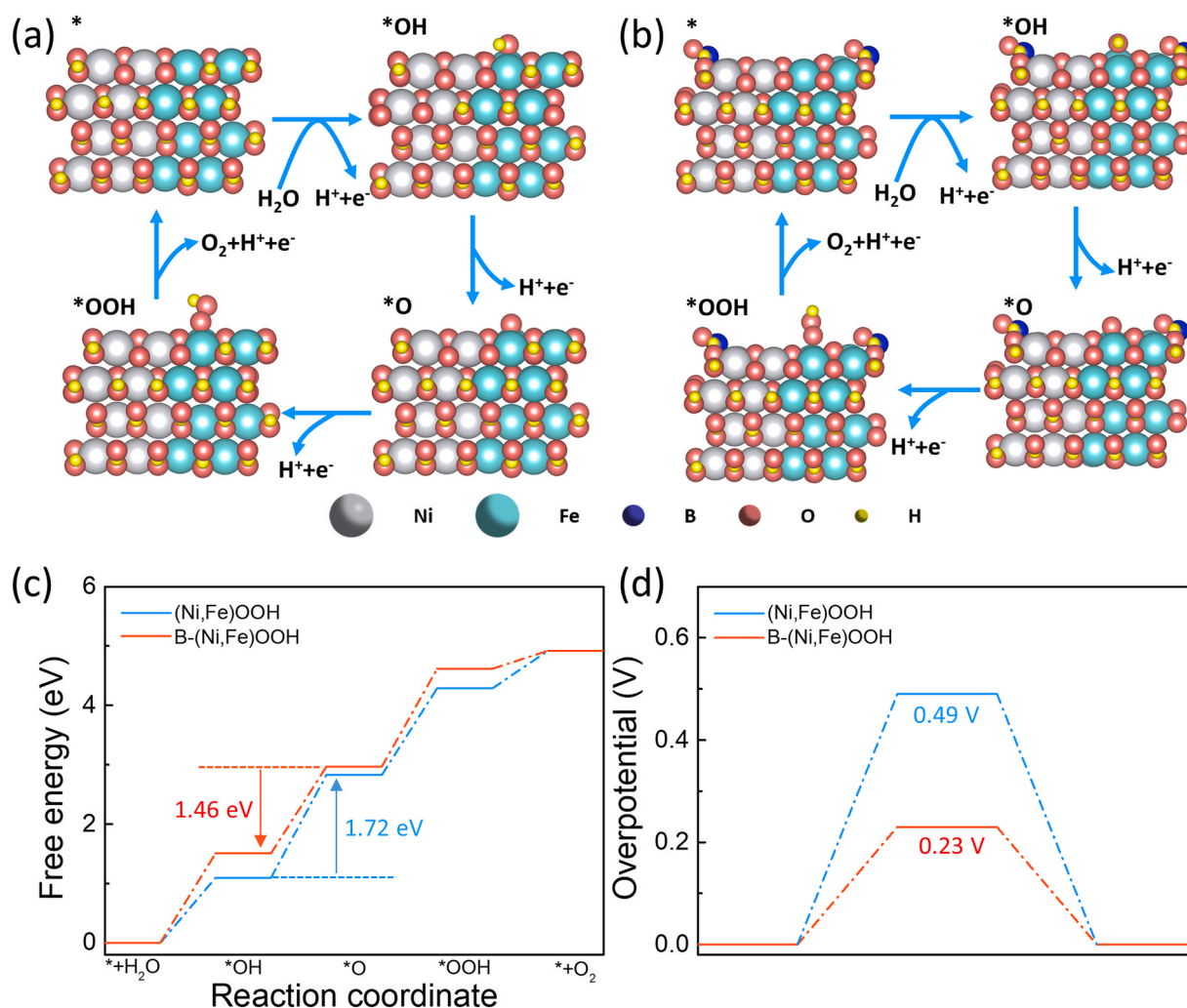
Fig. 5. Proposed OER processes *via* AEM on (a) (Ni,Fe)OOH and (b) B-(Ni,Fe)OOH. (c) Calculated free energy diagrams for (Ni,Fe)OOH and B-(Ni,Fe)OOH at a potential of 1.23 V. (d) Theoretical overpotentials of (Ni,Fe)OOH and B-(Ni,Fe)OOH for OER.

4. Conclusion

In summary, the highly active component B-(Ni,Fe)OOH was successfully fabricated on Ni_3N/NF *via* an ultra-fast chemical reduction method. Abundant active sites, the reduced free energy barrier of the rate-determining step, efficient electron transport and mass transfer, excellent corrosion resistance, and favorable hydrophilicity enable the resultant B-(Ni,Fe)OOH/Ni_3N/NF electrode to exhibit excellent electrocatalytic activity and stability for OER in both alkaline pure water and seawater media. Furthermore, the combined B-(Ni,Fe)OOH/Ni_3N/NF||Ru/(Fe,Ni)(OH)$_2$/NF electrolyzer achieves an extremely high current density of 1000 mA cm^{-2} at voltages of about 1.72 V and 1.76 V in 1 M KOH and alkaline seawater, respectively, superior to the benchmark IrO$_2$||Pt/C electrolyzer and most other reported electrolyzers. More importantly, when driven by a commercial Si solar cell, the B-(Ni,Fe)OOH/Ni_3N/NF||Ru/(Fe,Ni)(OH)$_2$/NF electrolyzer could achieve a high current (over 1000 mA) in alkaline seawater, which shows the great potential of its application as a photovoltaic-driven electrolyzer toward large-scale hydrogen production in seawater media at an industrially required current density.

CRediT authorship contribution statement

Yang Zhang: Formal analysis. **Xingxing Jiang:** Formal analysis, Data curation. **Fanghao Zhang:** Investigation, Data curation. **Brian McElhenny:** Methodology, Formal analysis. **Zhifeng Ren:** Writing – review & editing, Supervision, Conceptualization. **Yan Shen:** Writing – review & editing, Supervision, Funding acquisition, Formal analysis, Conceptualization. **Mingkui Wang:** Writing – review & editing, Supervision, Funding acquisition, Conceptualization. **Shuo Chen:** Methodology, Data curation. **Shaowei Song:** Writing – review & editing, Formal analysis, Conceptualization. **Yan Wei:** Writing – review & editing, Software, Investigation. **Xin Xiao:** Writing – review & editing, Writing – original draft, Software, Methodology, Investigation, Formal analysis, Data curation, Conceptualization.

Declaration of Competing Interest

The authors declare that they have no known competing financial interests or personal relationships that could have appeared to influence the work reported in this paper.

Data availability

No data was used for the research described in the article.

Acknowledgements

Appendix A. Supporting information

Supplementary data associated with this article can be found in the online version at doi:10.1016/j.apcatb.2024.123871.

References

[1] M. Dresselhaus, I. Thomas, Alternative energy technologies, Nature 414 (2001) 332, https://doi.org/10.1038/35104599.

[2] Q. Shi, C. Zhu, D. Du, Y. Lin, Robust noble metal-based electrocatalysts for oxygen evolution reaction, Chem. Soc. Rev. 48 (2019) 3181, https://doi.org/10.1039/C8CS00671G.

[3] J. Zhou, L. Yu, Q. Zhou, C. Huang, Y. Zhang, B. Yu, Y. Yu, Ultrafast fabrication of porous transition metal foams for efficient electrocatalytic water splitting, Appl. Catal. B Environ. 288 (2021) 120002, https://doi.org/10.1016/j.apcatb.2021.120002.

[4] X. Tian, P. Zhao, W. Sheng, Hydrogen evolution and oxidation: mechanistic studies and material advances, Adv. Mater. 31 (2019) 1808066, https://doi.org/10.1002/adma.201808066.

[5] C. Morales-Guio, L. Stern, X. Hu, Nanostructured hydrotreating catalysts for electrochemical hydrogen evolution, Chem. Soc. Rev. 43 (2014) 6555, https://doi.org/10.1039/C3CS60468C.

[6] Z. Wu, Y. Zhao, W. Jin, B. Jia, J. Wang, T. Ma, Recent progress of vacancy engineering for electrochemical energy conversion related applications, Adv. Funct. Mater. 31 (2020) 2009070, https://doi.org/10.1002/adfm.202009070.

[7] X. Xiao, X. Wang, B. Li, X. Jiang, Y. Zhang, M. Li, S. Song, S. Chen, M. Wang, Y. Shen, Z. Ren, Regulating the electronic configuration of ruthenium nanoparticles via coupling cobalt phosphide for hydrogen evolution in alkaline media, Mater. Today Phys. 12 (2020) 100182, https://doi.org/10.1016/j.mtphys.2020.100182.

[8] S. Dresp, F. Dionigi, M. Klingenhof, P. Strasser, Direct electrolytic splitting of seawater: opportunities and challenges, ACS Energy Lett. 4 (2019) 933–942, https://doi.org/10.1021/acsenergylett.9b00220.

[9] X. Zou, Y. Zhang, Noble metal-free hydrogen evolution catalysts for water splitting, Chem. Soc. Rev. 44 (2015) 5148–5180, https://doi.org/10.1039/C4CS00448E.

[10] S. Niu, W. Jiang, T. Tang, L. Yuan, H. Luo, J. Hu, Autogenous growth of hierarchical NiFe(OH)x/FeS nanosheet-on-microsheet arrays for synergistically enhanced high-output water oxidation, Adv. Funct. Mater. 29 (2019) 1902180, https://doi.org/10.1002/adfm.201902180.

[11] H. Lei, Q. Wan, S. Tan, Z. Wang, W. Mai, Pt-quantum-dot-modified sulfur-doped NiFe layered double hydroxide for high-current-density alkaline water splitting at industrial temperature, Adv. Mater. 35 (2023) 2208209, https://doi.org/10.1002/adma.202208209.

[12] L. Wu, L. Yu, B. McElhenny, X. Xing, D. Luo, F. Zhang, J. Bao, S. Chen, Z. Ren, Rational design of core-shell-structured CoPx@FeOOH for efficient seawater electrolysis, Appl. Catal. B Environ. 294 (2021) 120256, https://doi.org/10.1016/j.apcatb.2021.120256.

[13] W. Tong, M. Forster, F. Dionigi, S. Dresp, R.Sadeghi Erami, P. Strasser, A. Cowan, P. Farràs, Electrolysis of low-grade and saline surface water, Nat. Energy 5 (2020) 367–377, https://doi.org/10.1038/s41560-021-00851-4.

[14] L. Trotochaud, S. Young, J. Ranney, S. Boettcher, Nickel-iron oxyhydroxide oxygen-evolution electrocatalysts: the role of intentional and incidental iron incorporation, J. Am. Chem. Soc. 136 (2014) 6744–6753, https://doi.org/10.1021/ja502379c.

[15] Z. Huang, J. Song, Y. Du, S. Xi, S. Dou, J. Nsanzimana, C. Wang, Z. Xu, X. Wang, Chemical and structural origin of lattice oxygen oxidation in Co-Zn oxyhydroxide oxygen evolution electrocatalysts, Nat. Energy 4 (2019) 329–338, https://doi.org/10.1038/s41560-019-0355-9.

[16] G. Zhang, J. Zeng, J. Yin, C. Zuo, P. Wen, H. Chen, Y. Qiu, Iron-facilitated surface reconstruction to in-situ generate nickel-iron oxyhydroxide on self-supported FeNi alloy fiber paper for efficient oxygen evolution reaction, Appl. Catal. B Environ. 286 (2021) 119902, https://doi.org/10.1016/j.apcatb.2021.119902.

[17] M. Chen, S. Lu, X. Fu, J. Luo, Core-shell structured NiFeSn@NiFe(oxy)hydroxide nanospheres from an electrochemical strategy for electrocatalytic oxygen evolution reaction, Adv. Sci. 7 (2020) 190377, https://doi.org/10.1002/advs.201903777.

[18] L. Yu, L. Wu, B. McElhenny, S. Song, D. Luo, F. Zhang, Y. Yu, S. Chen, Z. Ren, Ultrafast room-temperature synthesis of porous S-doped Ni/Fe (oxy)hydroxide electrodes for oxygen evolution catalysis in seawater splitting, Energy Environ. Sci. 13 (2020) 3439–3446, https://doi.org/10.1039/D0EE00921K.

[19] Y. Kuang, M. Kenney, Y. Meng, W. Hung, Y. Liu, J. Huang, R. Prasanna, P. Li, Y. Li, L. Wang, M. Lin, M. McGehee, X. Sun, H. Dai, Solar-driven, highly sustained

[20] splitting of seawater into hydrogen and oxygen fuels, Proc. Natl. Acad. Sci. USA 116 (2019) 6624–6629, https://doi.org/10.1073/pnas.1900556116.

[20] P. Li, S. Zhao, Y. Huang, Q. Huang, B. Xi, X. An, S. Xiong, Adv. Energy Mater. (2023) 2303360, https://doi.org/10.1002/aenm.202303360.

[21] L. Wu, L. Yu, F. Zhang, B. McElhenny, D. Luo, A. Karim, S. Chen, Z. Ren, Heterogeneous bimetallic phosphide Ni2P-Fe2P as an efficient bifunctional catalyst for water/seawater splitting, Adv. Funct. Mater. 31 (2020) 2006484, https://doi.org/10.1002/adfm.202006484.

[22] C. Wang, M. Zhu, Z. Cao, P. Zhu, Y. Cao, X. Xu, C. Xu, Z. Yin, Heterogeneous bimetallic sulfides based seawater electrolysis towards stable industrial-level large current density, Appl. Catal. B Environ. 291 (2021) 120071, https://doi.org/10.1016/j.apcatb.2021.120071.

[23] X. Xiao, X. Wang, X. Jiang, S. Song, D. Huang, L. Yu, Y. Zhang, S. Chen, M. Wang, Y. Shen, Z. Ren, In situ growth of Ru nanoparticles on (Fe,Ni)(OH)2 to boost hydrogen evolution activity at high current density in alkaline media, Small Methods 4 (2020) 1900796, https://doi.org/10.1002/smtd.201900796.

[24] G. Kresse, J. Hafner, Ab initio molecular dynamics for liquid metals, Phys. Rev. B 47 (1993) 558–561, https://doi.org/10.1103/PhysRevB.47.558.

[25] J.P. Perdew, M. Ernzerhof, K. Burke, Rationale for mixing exact exchange with density functional approximations, J. Chem. Phys. 105 (1996) 9982–9985, https://doi.org/10.1063/1.472933.

[26] P.E. Blöchl, Projector augmented-wave method, Phys. Rev. B 50 (1994) 17953–17979, https://doi.org/10.1103/PhysRevB.50.17953.

[27] Y. Bai, Y. Wu, X. Zhou, Y. Ye, K. Nie, J. Wang, M. Xie, Z. Zhang, Z. Liu, T. Cheng, C. Gao, Promoting nickel oxidation state transitions in single-layer NiFeB hydroxide nanosheets for efficient oxygen evolution, Nat. Commun. 13 (2022) 6049, https://doi.org/10.1038/s41467-022-33846-0.

[28] H. Yang, L. Gong, H. Wang, C. Dong, J. Wang, K. Qi, H. Liu, X. Guo, B. Xia, Preparation of nickel-iron hydroxides by microorganism corrosion for efficient oxygen evolution, Nat. Commun. 11 (2020) 5075, https://doi.org/10.1039/C7CC05172G.

[29] W. Guo, D. Li, D. Zhong, S. Chen, G. Hao, G. Liu, J. Li, Q. Zhao, Loading FeOOH on Ni(OH)2 hollow nanorods to obtain a three-dimensional sandwich catalyst with strong electron interactions for an efficient oxygen evolution reaction, Nanoscale 12 (2020) 983–990, https://doi.org/10.1039/C9NR08297B.

[30] X. Li, P. Liu, L. Zhang, M. Zu, Y. Yang, H. Yang, Enhancing alkaline hydrogen evolution reaction activity through Ni-Mn3O4 nanocomposites, Chem. Commun. 52 (2016) 10566–10569, https://doi.org/10.1039/C6CC04141H.

[31] M. Chen, J. Qi, D. Guo, H. Lei, W. Zhang, R. Cao, Facile synthesis of sponge-like Ni3N/NC for electrocatalytic water oxidation, Chem. Commun. 53 (2017) 9566–9569, https://doi.org/10.1039/C7CC05172G.

[32] R. Wang, C. Xu, J. Lee, High performance asymmetric supercapacitors: new NiOOH nanosheet/graphene hydrogels and pure graphene hydrogels, Nano Energy 19 (2016) 10–221, https://doi.org/10.1016/j.nanoen.2015.10.030.

[33] X. Wang, W. Lu, Z. Zhao, H. Zhong, Z. Zhu, W. Chen, In situ stable growth of β-FeOOH on g-C3N4 for deep oxidation of emerging contaminants by photocatalytic activation of peroxymonosulfate under solar irradiation, Chem. Eng. J. 400 (2020) 125872, https://doi.org/10.1016/j.cej.2020.125872.

[34] H. Ren, X. Sun, C. Du, J. Zhao, D. Liu, W. Fang, S. Kumar, R. Chua, S. Meng, P. Kidkhunthod, L. Song, S. Li, S. Madhavi, Q. Yan, Amorphous Fe-Ni-P-B-O nanocages as efficient electrocatalysts for oxygen evolution reaction, ACS Nano 13 (2019) 12969–12979, https://doi.org/10.1021/acsnano.9b05571.

[35] S. Barwe, J. Weidner, S. Cychy, D. Morales, S. Dieckhöfer, D. Hiltrop, J. Masa, M. Muhler, W. Schuhmann, Electrocatalytic oxidation of 5-(Hydroxymethyl) furfural using high-surface-area nickel boride, Angew. Chem. Int. Ed. 57 (2018) 11460–11464, https://doi.org/10.1002/anie.201806298.

[36] D. Zhang, X. Kong, M. Jiang, D. Lei, X. Lei, NiOOH-decorated α-FeOOH nanosheet array on stainless steel for applications in oxygen evolution reactions and supercapacitors, ACS Sustain. Chem. Eng. 7 (2019) 4420–4428, https://doi.org/10.1021/acssuschemeng.8b06386.

[37] J. Jiang, F. Sun, S. Zhou, W. Hu, H. Zhang, J. Dong, Z. Jiang, J. Zhao, J. Li, W. Yan, M. Wang, Atomic-level insight into super-efficient electrocatalytic oxygen evolution on iron and vanadium co-doped nickel (oxy)hydroxide, Nat. Commun. 9 (2018) 2885, https://doi.org/10.1038/s41467-018-05341-x.

[38] M. Xie, Z. Xu, S. Duan, Z. Tian, Y. Zhang, K. Xiang, M. Lin, X. Guo, W. Ding, Facile growth of homogeneous Ni(OH)2 coating on carbon nanosheets for high-performance asymmetric supercapacitor applications, Nano Res. 11 (2017) 216–224, https://doi.org/10.1007/s12274-017-1621-4.

[39] C. Feng, M.B. Faheem, J. Fu, Y. Xiao, C. Li, Y. Li, Fe-based electrocatalysts for oxygen evolution reaction: progress and perspectives, ACS Catal. 10 (2020) 4019–4047, https://doi.org/10.1021/acscatal.9b05445.

[40] H. Xiao, H. Shin, W. Goddard III, 3rd, Synergy between Fe and Ni in the optimal performance of (Ni,Fe)OOH catalysts for the oxygen evolution reaction, Proc. Natl. Acad. Sci. USA 115 (2018) 5872–5877, https://doi.org/10.1073/pnas.1722034115.

[41] L. Wu, L. Yu, Q. Zhu, B. McElhenny, F. Zhang, C. Wu, X. Xing, J. Bao, S. Chen, Z. Ren, Boron-modified cobalt iron layered double hydroxides for high efficiency seawater oxidation, Nano Energy 83 (2021) 105838, https://doi.org/10.1016/j.nanoen.2021.105838.

[42] M. Cai, Q. Zhu, X. Wang, Z. Shao, L. Yao, H. Zeng, X. Wu, J. Chen, K. Huang, S. Feng, Formation and stabilization of NiOOH by introducing α-FeOOH in LDH: composite electrocatalyst for oxygen evolution and urea oxidation reactions, Adv. Mater. 35 (2023) 2209338, https://doi.org/10.1002/adma.202209338.